Co-delivery of NIR-II semiconducting polymer and pH-sensitive doxorubicin-conjugated prodrug for photothermal/chemotherapy

Dongsheng Yu[a,1], Yazhou Wang[a,1], Jifeng Chen [a,1], Shuang Liu [a], Shaohui Deng [a], Chengbo Liu [b], Iain McCulloch [c], Wan Yue [a, *], Du Cheng [a, *]

[a] PCFM Lab of Ministry of Education & Guangzhou Key Laboratory of Flexible Electronic Materials and Wearable Devices, School of Materials Science and Engineering, Sun Yat-sen University, Guangzhou 510275, PR China

[b] Research Lab for Biomedical Optics and Molecular Imaging, Shenzhen Key Lab for Molecular Imaging, Institute of Biomedical and Health Engineering, Shenzhen Institutes of Advanced Technology, Chinese Academy of Sciences, Shenzhen 518055, PR China

[c] University of Oxford, Department of Chemistry, Oxford, OX1 3TA UK

* Correspondence should be addressed to:
Du Cheng
Tel.: +86-20-84112172
Fax: +86-20-84112172
E-mail:chengdu@mail.sysu.edu.cn
Wan Yue
Tel.: +86-20-84112172
Fax: +86-20-84112172
E-mail:yuew5@mail.sysu.edu.cn
[1]These authors contributed equally to this work.

Keywords: NIR II photothermal therapy; Semiconducting polymer; Co-delivery; pH-sensitive drug release; Doxorubicin; Combined therapy

Abstract

Semiconducting polymer (SP) is a promising photothermal agent in the antitumor application, but the co-delivery of the second near-infrared window (NIR-II)-based SPs with chemotherapeutic drug (e.g., doxorubicin (DOX)) remains a challenge. Here, SPs were firstly improved via backbone and alkyl side-chain engineering, and afterward, SPs and pH-sensitive prodrug copolymer self-assembled into a nanoparticle for a photoacoustic (PA)-imaging guided combination of photothermal therapy and chemotherapy. SP-encapsulated nanoparticles exhibited a high photothermal conversion efficiency of 45% at a relatively low power level of NIR irradiation (0.3 W/cm^2 for 5 min). DOX was rapidly released in response to the acidic lysosomal environment. PA and fluorescence imaging confirmed that the photothermal therapy effectively drove DOX penetration inside tumor tissue, and it resulted in the killing of the surviving tumor cells from hyperthermia. The synergistic effect of SP-based photothermal therapy and DOX-induced chemotherapy was verified *in vivo*. Overall, the co-delivery of the SP and DOX using pH-sensitive nanoparticles represents a feasible strategy for photothermal therapy with potentially synergistic drug effects.

Abbreviation: Semiconducting polymers, SPs; PEG-PAsp(BzA-*co*-DIP-*co*-DOX), PADD; PEG-PAsp(BzA-*co*-DOX), PABD; PEG-PAsp(DIP-*co*-BzA) without DOX, PADB; PADD NPs, nanoparticles assembled with PADD polymers; PADB NPs, nanoparticles assembled with PADB polymers; PABD NPs, nanoparticles assembled with PABD polymers; PADD@SPs, nanoparticles assembled with PADD polymers and SPs; PABD@SPs, nanoparticles assembled with PABD polymers and SPs; PADB@SPs, nanoparticles assembled with PADB polymers and SPs.

1. Introduction

Compelling evidence confirmed the promising applications of photothermal therapy (PTT) due to its non-invasiveness and spatial control features [1-3]. Photothermal agents, including inorganic nanomaterials, small molecular organic dyes, and organic nanoparticles convert absorbed photons into heat, spatially killing tumor cells with negligible damage to surrounding normal tissues [4-13]. Inorganic nanomaterials (e.g., gold nanoparticles, palladium nanoparticles, metal sulfide nanoparticles, and carbon derivatives) show effective antitumor effect under Near Infrared (NIR) irradiation [6, 7]. Compared to inorganic nanomaterials, organic dyes (e.g., cyanine dyes and porphyrin derivates) showed better photothermal conversion capacity and superior antitumor therapeutic effects due to their size-independent photophysical and biodegradable features [8-10, 14, 15]. Recently, photothermal therapy based on semiconducting polymer (SP) nanoparticles has shown promising results as an antitumor treatment due to its inherent advantages, including noninvasiveness, high photostability, oxidative tolerance, good biocompatibility, and controllable size [11, 12, 16, 17]. However, two issues with SP-based PTT remain: i) SPs with suitable photothermal properties are limited; ii) uncontrolled release of small molecules drugs co-delivered with SPs has a negative effect on the outcome of treatment.

Since the opto-electrical property and photothermal conversion efficiency are associated with the molecular structure of SPs, backbone and side-chain engineering are two mainly used approaches to optimize SPs. For the backbone engineering, precisely choosing the electron-rich and/or electron-deficient motifs was used to construct variable SPs [13, 18]. For instance, the SPs copolymer incorporating electron acceptor fullerene derivative $PC_{70}BM$ with electron donor dithiophene-*alt*-benzothiadiazole showed superior PTT therapy and PA imaging due to its enhanced charge carrier mobilities [19]. Isoindigo, which shows strong electron-deficient character due to the two electron-withdrawing lactam moieties, has been extensively applied to build SPs for high-performance field-effect transistors (FETs), solar cells, and thermoelectric applications [20, 21]. In our previously reported work, thiophene isoindigo (TIID) was designed and prepared to eliminate the steric effect of repeating unit to further promote planarity by maximizing the π-conjugation and enhancing close intermolecular contacts [20]. TIID building block with branched 2-occtyldodecyl side chain was copolymerized with 2,1,3-benzothiadiazole (BT) to form TIID-BT SPs. The TIID-BT SPs showed a very low optical bandgap in the second near-infrared window (NIR-II) range and significant ambipolar behavior in the FETs with hole and electron mobilities up to 0.1 cm^2/Vs. Thus, the outstanding NIR absorption properties of this copolymer may present a potential application in the biomedical area [22]. Side-chain engineering is another effective method to optimize SPs. The length, size, topology, and polarity of side-chain grafted to the backbone play important roles in the molecular weight, molecular packing, and thin-film morphology, and further influence the final device performances [23]. Branched alkyl side chains, which are the most widely used solubilizing groups of SPs, also play important roles in light energy conversion efficiency [23, 24]. Besides, the molecular weight of SPs is a key factor in determining their optical-electrical, morphological, and performance properties [25]. Compared to the low molecular weight polymer, the high molecular weight polymer shows an enhanced extinction coefficient absorption [26]. In addition, the SPs with a maximum absorption peak at the second NIR window (NIR-II, 960 nm-1,700 nm) have shown a photothermal effect even in the deep tumor tissue due to the deep tissue penetration ability of the NIR-II laser [27, 28]. However, the influence of the molecular weights and side-chain of the SPs on the photothermal/chemotherapy has not been reported yet. Therefore, owing to the long-wavelength NIR absorption with high intensity and molecular structure modification that is easily tuned through changing the length of the side chain, TIID-BT is a promising SP for photothermal therapy.

Most developed SPs are highly hydrophobic due to their phenyl, heterocyclic group-rich structures, and hydrophobic side chains. Some amphiphilic polymers such as polyethylene glycol-poly(2-hexoxy-2-oxo-1,3,2-dioxaphospholane), namely PPG-PHEP, PEG-DSPE, and PEG-PPG-PEG with hydrophilic ethylene glycol block have been developed to encapsulate SPs for in vivo therapeutic applications [2, 29, 30]. The non-homogeneous distribution of the intratumor NIR light intensity results in some tumor cells survived from NIR-induced hyperthermia [31, 32]. Co-delivery of photothermal agents with small-molecule chemotherapeutic drugs is a promising approach to address this challenge via the synergistic effect of two different means

[33-35]. The amphiphilic polymer-based nanoplatforms have been used to co-deliver two or multiple drugs to achieve significant synergistic antitumor effects [36-38]. Gold shell-coated polymeric vesicles and amphiphilic SPs have been utilized to deliver chemotherapeutic drug doxorubicin (DOX), generating NIR-triggered hyperthermia to drive DOX penetration inside the tumor tissue and thereby killing tumor cells survived from PTT therapy [4, 31]. Pro-chemotherapeutic drugs were activated by PTT-induced inflammation to exert photothermal-chemotherapy [34]. In addition, polydopamine and organic dyes (e.g., indocyanine Green (ICG) and new indocyanine green (IR820)) have been also used as photothermal agents to perform photothermal-chemotherapy [35]. However, the controlled release of co-delivered chemotherapeutic drugs has not been investigated thoroughly.

Controlled release of drugs is desired to reduce drug loss in the bloodstream and rapidly release the drug from nanoparticles in tumor cells. Controlled DOX releases triggered by intracellular stimuli have been achieved by reducing disulfide bonds in the cytoplasm, by the dissolution of the pH-sensitive interlayer of nanoparticles in the acidic lysosomal environment [39-41]. When DOX is released in tumor tissue, it should penetrate inside tumor tissue to kill tumor cells escaped from PTT therapy. External stimuli (e.g., NIR and ultrasonic irradiation) have been used to promote small-molecule drugs penetration inside tumor tissues *via* thermal and cavitation effects [4, 42], respectively. Therefore, a combination of stimuli-triggered drug release and NIR irradiation-drove drug penetration is desirable to achieve a significant synergistic antitumor effect.

The objectives of this study are (i) to compare the photothermal conversion efficiency of several TIID-BT SPs with various molecular weights and different lengths of alkyl side chain, and (ii) to develop a pH-responsive nanoparticle encapsulating SPs and DOX, which allows a controlled release and deep penetration of DOX in tumor tissue to achieve photothermal-chemotherapy with synergistic effect (Figure 1).

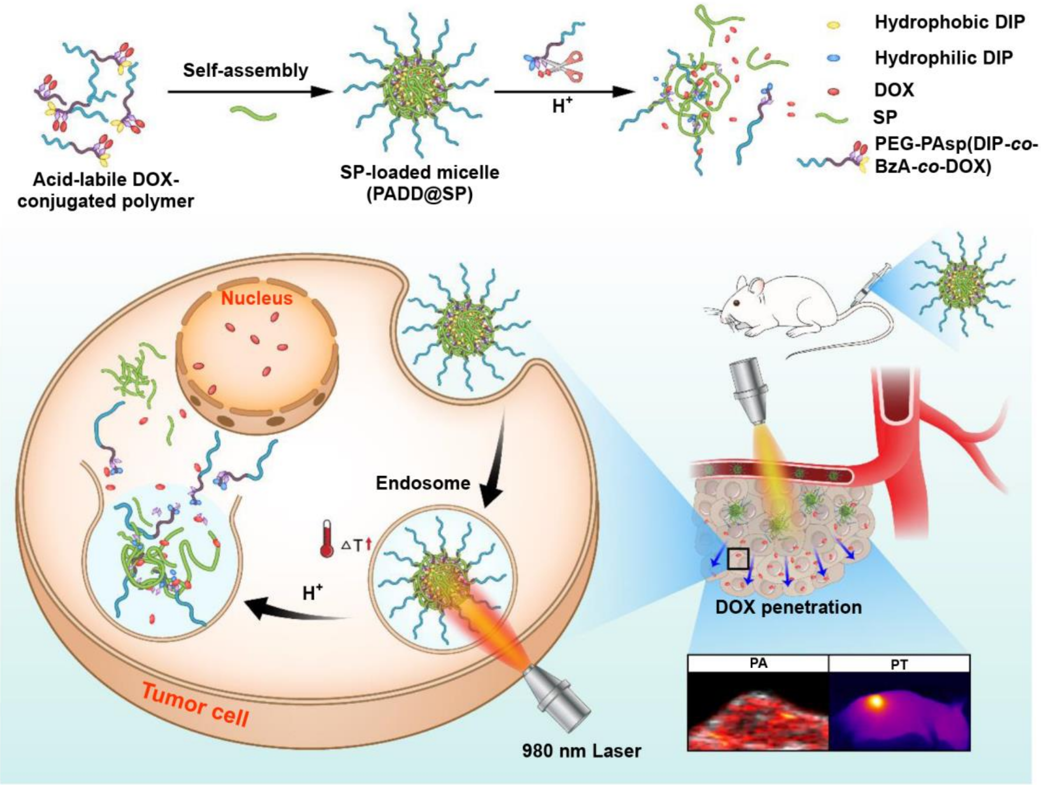

Figure 1. Schematic of the preparation, delivery, and intracellular drug release of NIR- and pH-dual responsive nanoparticles incorporating semiconducting polymers (SPs) and DOX. Nanoparticles are prepared by self-assembly of micelles using pH-sensitive copolymer PEG-PAsp(DIP-*co*-BzA-*co*-DOX) encapsulating SPs. Nanoparticles are internalized by tumor cells in which lysosome DOX are released from nanoparticles by breaking the hydrazine bond. Upon NIR irradiation, SPs generate hyperthermia to kill tumor cells. The NIR-induced hyperthermia also drives DOX penetration inside the tumor tissue to kill tumor cells survived from the photothermal therapy (PTT). Thus, co-delivery of SPs and DOX exhibits a synergistic antitumor effect. PA and PT imaging indicates photoacoustic and photothermal imaging.

2. Materials and methods

2.1 Materials and reagents

N,N-Dimethylformamide (DMF, 99.8%) was ordered from J&K. Dimethylsulfoxide (DMSO, J&K) was dried through CaH_2 and then distilled under atmospheric conditions. N,N-Diisopropylethylenediamine (DIP, 99.8%), benzylamine (BzA) J&K), chloroform ($CHCl_3$), and dichloromethane (CH_2Cl_2, 99.9%) were purchased from J&K. α-Methoxy-ε-hydroxy-poly(ethylene glycol) (mPEG-OH, Mn: 2 kDa) was purchased from Fluka (Buchs, Switzerland). Triethylamine (TEA) was purchased from Sigma-Aldrich, St. Louis, MO, USA. Hydrazine hydrate (98%) was purchased from Aladdin. The monomers were purified by column chromatography using silica gel (General-Regent, 200-300 mesh). Doxorubicin hydrochloride (DOX·HCl) was purchased from Dalian Meilun, Biotech Co., Ltd, China. Dialysis bags (3500 Da) were purchased from Guangzhou Anjin Biotechnology Co. Ltd, China. 1,1-dioctadecyl-3,3,3,3-tetramethylindotricarbocyanine iodide (DiR) was obtained from J&K Chemical Reagent Co. (Beijing, China). Trypsin-EDTA, cell culture medium, and fetal bovine serum were purchased from Life Corporation (Gibco, USA). The Annexin-V FITC and PI Apoptosis and 3-(4,5-Dimethyl-thiazol-2-yl)-2,5-diphenyltetrazolium bromide (MTT) Kits were from KeyGEN Biotechnology Company (Nanjing, China). The A549 human lung adenocarcinoma cell line was purchased from Cold Spring Biotech Corp (Shanghai, China) and cultured in Dulbecco's Modified Eagle Medium (DMEM) with 10% fetal bovine serum and 1% antibiotics (penicillin and streptomycin) in an atmosphere with 5% CO_2 and 95% humidified air at 37 °C.

2.2 Preparation of SP-loaded polymeric micelles (PADD@SPs) and PADD NPs

The detailed synthesis of TIID-BT SPs, DOX-grafted block polymer monomethoxypoly(ethylene glycol)-poly(N-(N',N'-diisopropylaminoethyl)-co-benzylamino-co-DOX)aspartamide (PEG-PAsp(DIP-*co*-BzA-*co*-DOX), referred to here as PADD), monomethoxypoly(ethylene glycol)-poly(N-benzylamino-*co*-DOX) aspartamide (PEG-PAsp(BzA-*co*-DOX)), referred to here as PABD) , and monomethoxypoly(ethylene glycol)-poly(N-(N',N'-diisopropylaminoethyl)-co-benzylamino)aspartamide (PEG-PAsp(DIP-*co*-BzA), referred to here as PADB) without DOX groups are described in the Supporting Information. In addition, the synthesis of pH-insensitive copolymer monomethoxypoly(ethylene glycol)-poly (caprolactone) (PEG-PCL) is described in Supporting Information.

The SP-loaded micelles PADD@SPs were prepared from the copolymer PADD and SPs as outlined in Figure 1. In brief, SPs (0.5 mg) and polymer PADD (5 mg) were dissolved in 1 mL of THF: DMSO (9:1) solution. Under ultrasonic agitation, the solution was added dropwise into PBS (pH 7.4, 20 mM) followed with dialysis (molecular weight cut off (MWCO): 3.5 kDa) against PBS (pH 7.4, 20 mM) for 48 h at room temperature. The external buffer solution was changed every 6 h. The resulting micelle solutions were lyophilized and weighed. PADD NPs without SPs, PADB@SPs without DOX, PABD@SPs without DIP group nanoparticles were prepared according to the similar procedure.

Amounts of SPs and DOX in the micelles were determined with a UV-Vis spectrophotometer (UV-3150, Shimadzu, Japan). Briefly, the absorbances of various concentrations of SPs in THF were measured at 960 nm to generate a calibration curve. Predetermined amount of the freeze-dried micelle (e.g., 5 mg) was dissolved in THF (1.0 mL), and the absorbances at 960 nm of different SPs in the THF solution were measured. Then, the mass of SPs was calculated by referring to the pre-established calibration curve. The SPs loading content (DLC) and efficiency (DLE) of the micelles was calculated using the following formulas: DLC = (the mass of SPs/the mass of micelle) ×100%, DLE = (the mass of SPs in the micelle/the mass of SPs in feed) ×100%. The loading content of DOX was calculated by the same procedure.

2.3 Characterization

For the monomers of semiconducting polymers, ^{1}H-nuclear magnetic resonance (^{1}H-NMR) and ^{13}C-NMR were recorded in $CDCl_3$ with a 400 M Bruker Avance III spectrometer (Bruker Biospin, Rheinstetten, Germany) at room temperature. For semiconducting polymer, ^{1}H-NMR were recorded at the following procedure: the semiconducting polymers were dissolved in 1,1,2,2-tetrachloroethane-d_2 (TCE-D_2), ^{1}H-NMR of semiconducting polymers were recorded in TCE-D_2 with a 500 HMz Bruker Avance III spectrometer (Bruker Biospin, Rheinstetten, Germany). Absorption spectra of semiconducting polymers were measured with an UV-Vis spectrophotometer (Agilent Technologies Co.Ltd, Cary 5000/6000i, USA) using a quartz cell of 1 cm wide in chloroform with a concentration of 1.0 $\times 10^{-5}$ M. For amphiphilic polymer, a 400 MHz spectrometer (Varian Unity Anova 400, Palo Alto, CA, USA) was used to perform the ^{1}H-NMR spectra analysis when DMSO-d_6 was used as solvent. The number average molecular weight (Mn) and polydispersity index (PDI) distribution of polymers were analyzed by using a gel permeation chromatography (GPC, Agilent 1260 Infinity II, Waldron, Germany) system and calculated against polydispersity polystyrene standard. The eluting was chlorobenzene and used at a flow rate of 1 mL/min under 80 °C. Fourier transform infrared spectra (FTIR) were conducted on a Fourier transform infrared spectrometer (Nexus 670, Thermo Electron Nicolet, Thermo Electron Co., Madison, WI, USA) using KBr pellet. Transmission electron microscopy (TEM) was performed to record the nanoparticles' morphologies using a Philips CM120 transmission electron microscope (Philips, Eindhoven, Netherlands) at 100 kV. 5 μL of sample solution (5mg/mL) was dropped on a copper grid coated with amorphous carbon. The ultraviolet absorption spectrum and infrared absorption spectrum of the materials were recorded on an UV-visible-near-infrared spectrophotometer (UV-3600, Shimadzu, Japan). The hydrodynamic sizes of the micelles were recorded using a dynamic light scattering instrument (DLS, Nano ZS instrument, Malvern Instruments Ltd, UK) at 25 °C. The data was determined on the auto-correlator mode at a detection angle 90° to the scattered light. The NIR thermal imaging was performed using an infrared thermal imager Fluke Ti32 (Fluke Corporation, USA).

2.4 *In vitro* photothermal study

200 μL of PADD@SPs solutions in 1 × PBS (pH 7.4) at concentrations of 5, 10, 20, 40, or 60μg/mL were irradiated with a 980 nm laser at a power density of 0.3 W/cm^2. The temperature of the solution was monitored every 60 s by using a digital thermometer during both the photothermal heating (10 min) and natural cooling periods (15 min). The photothermal conversion efficiency under NIR irradiation of 0.3 W/cm^2 power density was calculated according to previously reported method [43] . The total energy balance for the system is expressed by equation: $\eta=[hs(T_{max}-T_{surr})-Q_{dis}]/I(1-10^{-A\lambda})$, where η indicates the photothermal conversion efficiency, h indicates the heat transfer coefficient, S indicates the surface area of the container, T_{surr} indicates ambient temperature of the surroundings, T_{max} indicates the equilibrium temperature of SPs solution, Q_{dis} that indicates the heat associated with the light absorbance of the solvent is measured independently to be 29.72 J/s by using pure water without SPs, Aλ indicates the absorbance of SPs at the wavelength of 980 nm (e.g., $A\lambda_{L\text{-}SP\text{-}C10}$=2.11), and I indicates incident laser power (0.3 W/cm^2). In the equation, hs is unknown for calculation. The calculations of η, hs, and Qdis are described in detail in Supporting Information.

For the photostability study, 200 μL of the PADD@SPs solution (70 μg/mL) was irradiated with a 980 nm laser at a power density of 0.3 W/cm^2. The photothermal heating (10 min) and natural cooling (another 15 min) cycles were repeated ten times to evaluate the photostability of PADD@SPs.

2.5 Cellular uptake and intracellular distribution

To monitor the nanoparticles, the coumarin 6 (Cr6) in lieu of SPs was encapsulated in the cores of micelles and emitted green fluorescence. The cell nucleus was stained blue with Hoechst 33324. Cells were plated in a glass-bottom well at a density of 1×10^3 cells per well. After incubation overnight, the cells were treated with various nanoparticle with or without DOX via pH-sensitive hydrazone bond (i.e., PADD@Cr6 and PADB@Cr6). The concentrations of DOX and Cr6 were 8 and 0.2 μg/mL, respectively. After incubation for different times (e.g., 6 h, 12 h, and 24 h), cells were washed three times with 1×PBS. The fluorescence from DOX, Cr6, and nucleus was recorded using a confocal laser scanning microscope (CLSM, Leica SP8, Germany). To quantify the cellular uptake of the PADD@Cr6, a flow cytometer (Attune NxT, Invitrogen, America) was used. In brief, A549 cells were seeded in a 12-well plate at a density of 5×10^4 cells per well. After culturing with different micelles with/without SPs, cells were washed three times with 1×PBS and detached with trypsin (0.25%). The cells that was resuspended in 300 μL 1×PBS were subjected to flow cytometry assay.

2.6 Cell viability and apoptosis assays

The A549 cells were seeded in 96-well plates at a density of 6×10^4 cells per well and then cultured in 200 μL DMEM for 24 h. After being washed with 1 × PBS (pH 7.4), the cells were treated with different micelles formulations (i.e., PADD@SPs, PADD NPs, PADB@SPs, and PADB NPs). The polymer concentrations in the PADB NPs and PADB@SPs were 50, 100, 200, 400, and 800 μg/mL, and the DOX concentration in the PADD NPs and PADD@SPs were 2, 4, 6, 8, and 32 μg/mL, respectively. The cytotoxicity of different micelles (i.e., PADB@SPs and PADD@SPs) was investigated with/without NIR irradiation. After micelle solutions were added to the culture medium, the cells were cultured for further 24 h. Then, the culture medium was removed and cells were gently washed with 1×PBS. Fresh DMEM culture medium (100 μL) containing 10 μL MTT solution (0.5 mg/mL) were added to each well. After cells were incubated for another 4 h, the absorbance of cell culture at 570 nm was measured using a microplate reader (Biotek, Winooski, VT, USA) to determine cell viability.

The percentage of apoptotic cells was quantified using flow cytometry assay. Cells were cultured and collected as described previously. The cells that received various treatments were detached using 0.25% trypsin. The detached cells were harvested through centrifugation and resuspended in 300 μL of 1×PBS for flow cytometry assay. The excitation/emission wavelengths of DOX, Cr6, and DAPI were 550/580 nm, 490/520 nm, and 405/455 nm, respectively.

2.7 Combination index analysis

To determine the synergistic effect of SP/NIR irradiation-based photothermal therapy in combination with DOX-based chemotherapy *in vitro*, A549 cells were seeded in 96-well plates at a density of 6×10^4 cells per well. After 24 h incubation, cells were treated with different concentrations of SPs (e.g., 2, 4, 6, 8, 10μg/mL), DOX (e.g., 2, 4, 8, 16, 32 μg/mL), and combinations of SPs (e.g., 4 μg/mL) and DOX (e.g., 2, 4, 8, 16, 32μg/mL), respectively. After 48 h, cell viability was determined according to previously mentioned MTT assay. The synergism of SP-based photothermal therapy and DOX-based chemotherapy was analyzed by calculating the combination index (CI) according to the Chou-Talalay method [44]. The CI values were calculated through the CompuSyn software, where CI < 1, $= 1$, and >1 indicate synergistic, additive, and antagonistic effects respectively.

2.8 Animal modeling

Subcutaneously implanted tumor model was established using 6-weeks-old BALB/c nude mouse (female, 15-20 g body-weight). Briefly, mice were anesthetized with Chloral hydrate (100 mg/kg) and placed in a bench holdfast. A549 cells (1×10^6 per mouse) suspended in 200 μL serum-free RPMI 1640 medium were subcutaneously injected in upper thighs. When tumor grew up to 75 mm^3, the mice were treated with different formulations. Studies involving animals were approved by Animal Care and Use committee of Sun Yat-Sen University approved by the Animal Ethics Committee of the People’s Republic of China.

2.9 *In vivo* nanoparticle biodistribution

The biodistribution of nanoparticles was evaluated in the A549 xenografts mice using a small animal *in vivo* fluorescence imaging system (In vivo Imaging System FX Pro, Carestream Health Inc., New Haven, CT, US). To monitor the distribution of SPs, the fluorescence dye dialkylcarbocyanines (Dir) was used in the place of SPs. When the tumor volume reached approximately 100 mm^3, the nanoparticles loading Dir (i.e., PADD@Dir) (Dir dose: 1 mg/kg body-weight) were intravenously injected into mice. Fluorescence imaging was conducted at predetermined time points (i.e., 4, 6, 10, 24, and 48 h after drug injection). Mice were sacrificed at 48 h after drug injection, and then tumors as well as major organs were subjected to *ex vivo* fluorescence imaging.

To evaluate the photothermal effect of pH-sensitive PADD@SPs and pH-insensitive PEG-PCL@SPs, the mice bearing subcutaneously transplanted A549 tumors about 100 mm^3 were subjected to infrared imaging. 200 μL of nanoparticle solutions (i.e., PADD@SPs and PEG-PCL@SPs in PBS solution) were injected via the tail vein at a SPs dose of 2 mg/kg body-weight, respectively. At a 6 h time point after nanoparticles injection, tumors were irradiated with a 980 nm laser at power density of 0.3 W/cm^2 for 1, 2, 3, 4, and 5 min, respectively. The mice injected with PBS solution were used as the control group. Temperature values of tumor areas were recorded using a FLIR SC300-Series infrared thermal imager (FLIR Systems, Wilsonville, OR, USA).

For the PA imaging capacity of tumor receiving PADD@SPs nanoparticle, a custom-built photoacoustic imaging system from Shenzhen Institutes of Advanced Technology was used. This system has two main components: laser section (a nanosecond pulsed OPO laser source, Spitlight 600 OPO) from Innolas Laser Co. Ltd (Krailling, Germany) for photoacoustic signal excitation and imaging section (an open-platform ultrasound imaging system, Vantage 64 LE) form Verasonics Co. Ltd (Kirkland, WA) for receiving and processing the signals from photoacoustic probe. Laser at a wavelength of 980 nm was generated with a tunable laser operating and integrally transmitted into the transducer through fiber optic bundles. After anesthetization with isoflurane, mice were placed on a heat pad by which the electrocardiogram (ECG), respiration rate, and body temperature were monitored. The ultrasound and photoacoustic signals were recorded before and after *i.v.* injection of PADD NPs (SPs dose: 2 mg/kg body weight). Reconstruction of the PA images was performed with OsiriX imaging software (OsiriX Lite, Switzerland).

To analyze the penetration of nanoparticles in tumor tissue, the GFP (green fluorescence protein) gene recombinant human A549 cells (A549-GFP) were constructed to *in vivo* image tumor cell with CLSM system according to the literatures [4]. The A549-GFP tumor cells were subcutaneously transplanted at the auricle areas of mice. When the xenografted tumor grew to ~20 mm^3 suitable for imaging, the PADD@SPs were administrated *via* tail vein. At a time point of 8 h post injection, a 980 nm laser at a power density of 0.3 W/cm^2 was utilized to irradiate the tumor areas for 5 min. Then, the mice were placed on the bracket of CLSM system. To localize DOX position in tumor tissue, the tumor microvessels were observed under bright field mode. The fluorescence of A549-GFP cell and DOX were recorded under fluorescence mode (DOX: Ex/Em = 550/580 nm; GFP: Ex/Em = 490/520 nm).

2.10 *In vivo* synergistic anticancer effect

When tumor volumes reached 70 mm^3, the mice were randomly divided into six groups: PBS, free DOX, PADD NPs, PADB@SPs/NIR, and PADD@SPs/NIR groups. The PADD NPs treatment indicates that mice treated with PADD nanoparticles without SPs; PADD@SPs treatment indicates that mice treated with PADD nanoparticles incorporating SPs; PADB@SPs/NIR treatment indicates that mice treated with PADB nanoparticles lacking DOX under NIR irradiation; PADD@SPs/NIR treatment indicates that mice treated with PADD@SPs with DOX and SPs under NIR irradiation.

The mice were treated with different formulations through a tail vein injection every two days. If applied, the doses of SPs and DOX were 2 and 4 mg/kg body weight, respectively. The tumor volumes of mice were measured every 2 days according to the following formula: Volume = length × width^2 / 2, where length and width were the longest and the shortest diameter of the tumor. On day 32 after beginning of treatment, the mice were sacrificed, and the excised tumor tissues were weighted, photographed, and dissected.

To evaluate the pathological changes and tumor apoptosis after treatments, the tumor tissue sections were subjected to hematoxylin and eosin (H&E) and TUNEL analyses. Tumor tissues embedded in paraffin were sectioned into samples of 2 μm thick. Then, the tissue sections were subjected to H&E staining and TUNEL assay according to standard protocol. For H&E staining, after deparaffinization with xylene and hydration with 100%, 90%, 80%, and 70% ethanol, sections were subjected to H&E staining and then covered with Rhamsan$^@$ gum. The prepared tumor sections were observed under a microscope. For TUNEL assay, the FragEL^{TM} DNA Fragmentation Detection Kit was applied to detect apoptotic cells. Briefly, after permeabilization with proteinase K, the tumor tissue sections were immersed in 3% H_2O_2/MeOH to inactivate endogenous peroxidase. Fragmented DNA with 3′-OH in the apoptotic cells were marked using terminal deoxynucleotidyl transferase (TdT) at 37 °C for 1.5 h. Then, the apoptotic cells were stained with a commercially available DAB kit and recorded using a Pathology Imaging System (PerkinElmer Vectra, Waltham, MA, US).

2.11 Statistical analysis

Data were expressed as means ± standard deviation (SD). Statistical differences were performed with the one-way ANOVA analysis (SPSS software, version 13.0, SPSS Inc) to calculate *P* values (* $p < 0.05$, ** $p < 0.01$, *** $p < 0.001$).

3. Results and discussion

3.1 Synthesis and characterization of semiconducting polymer

To optimize the photothermal conversion efficiency, three TIID-BT SPs (i.e., L-SP-C10, SP-C10, and SP-C8) with different average molecular weights (Mn) and branched alkyl side-chain lengths were synthesized and characterized (**Figure 2a** and **S1-7**, Scheme **S1** and **2**, and **Table S1**). The L-SP-C10 and SP-C10 have branched chains of 2-decyltetradcane, and SP-C8 bears a shorter branched 2-octyldodecyl side chain at the amide position of thiophene isoindigo. These polymers were characterized by using high-temperature proton nuclear magnetic resonance (^{1}H-NMR) spectra (**Figure S1, S3,** and **S5**). The characteristic broad peaks at 7.0-9.0 ppm are attributed to *H* of the aromatic ring including thiophene and benzothiadiazole, while multiple peaks ranging 1.7 to 5.0 are *H* of the alkyl chain, and the broad and non-splitting peaks indicat the strong aggregation of polymers. The molecular weights of SPs were determined by high-temperature gel permeation chromatography (GPC) with chlorobenzene as the eluting agent at 80 °C relative to the monodisperse polystyrene standards. The SP-C10 and SP-C8 exhibited higher number-average molecular weights (Mn) of 19.6 and 26.0 kDa with polydispersity indexes (PDI) of 2.83 and 2.54 (**Figure S5**), respectively. The low molecular weight polymer L-SP-C10 shows a low Mn of 3.0 kDa with a PDI of 4.18 (**Figure S7** and **Table S1**). All these polymers L-SP-C10, SP-C10, and SP-C8 show good solubility in commonly used organic solvents (e.g., tetrahydrofuran, chloroform and toluene) due to the small fused aromatic system of thiophene IID and long branch side chains. Notably, the high solubility of these polymers is in favor of the nanoparticles self-assemble with the amphiphilic copolymer, by which the hydrophobic semiconducting polymers can be encapsulated in the core of nanoparticles (**Figure 1**).

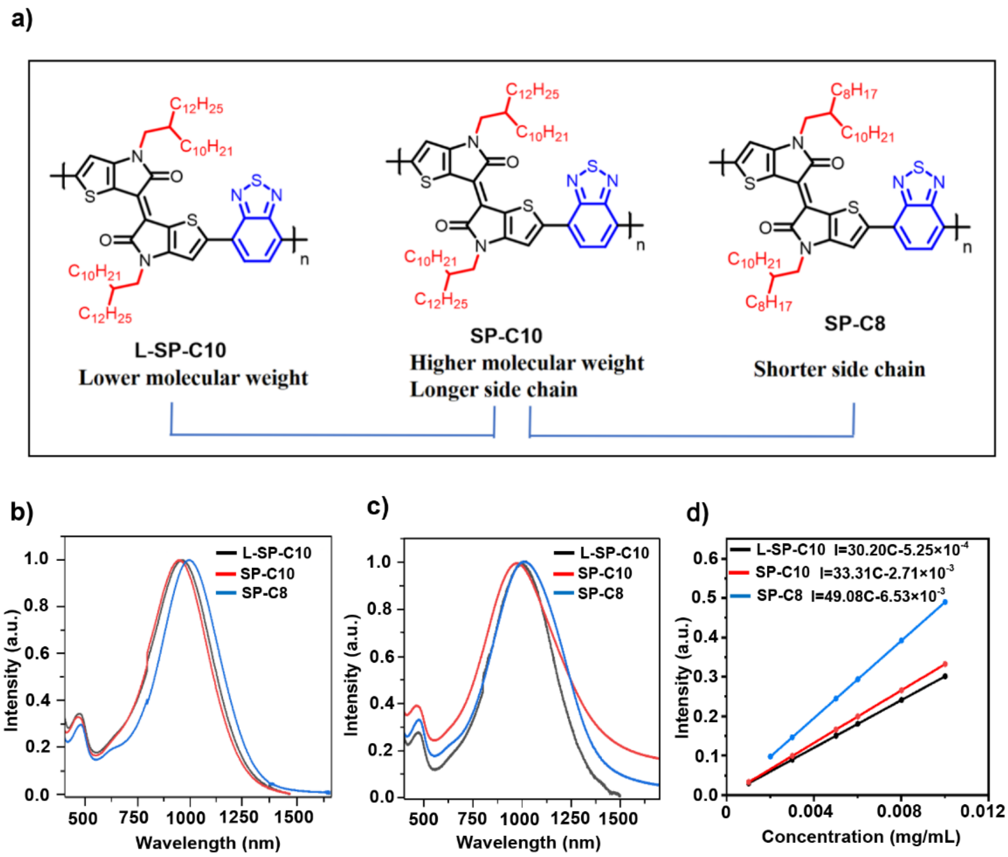

Figure 2. Structures and characterizations of different SPs. (a) Structures of different SPs, (b) and (c) Normalized UV-vis-NIR absorption spectra of various SPs in the chloroform solutions and films, and (d) Extinction coefficient of SPs in the chloroform solution.

The UV-vis-NIR absorption of SPs displays a dual band absorption feature in chloroform solutions (**Figure 2b**). The absorption band with very low intensity at 400-525 nm is ascribed to the π-π* transition, and the stronger absorption band with much higher intensity at 525-1200 nm refers to the electron delocalization along the backbone, indicating the formation of a large π-conjugated thienoquinoid structure when the thiophene was incorporated into the system [19, 20]. Absorption peaks of SP-C10 in the solution and the thin film show an interesting blue-shift in comparison with the L-SP-C10, which may be attributed to their aggregation ability and packing motif. Compared with the L-SP-C10 and SP-C10, SP-C8 shows a significantly red-shifted absorption spectrum, both in the solution and the solid states. The red-shifted absorption attributed to the fact that the shorter branch side chain of SP-C8 led to a more ordered structure and more planar backbone, both in the solution and the solid states. Compared with the absorption spectra of all the three SPs in solution, the absorption spectra of SPs in the solid state were all red-shifted, indicating aggregations and/or orderly π-π stacking formed in the solid state (**Figure 2c**). An extinction coefficient of 30.20 $L\cdot g^{-1}\cdot cm^{-1}$ at the wavelength of 970 nm for L-SP-C10 was calculated when correlating the absorbance with the concentration of SPs in chloroform. SP-C10 showed a higher extinction coefficient of 33.31 $L\cdot g^{-1}\cdot cm^{-1}$ at the wavelength of 957 nm due to the higher molecular weight, whereas SP-C8 showed a much higher extinction coefficient of 49.08 $L\cdot g^{-1}\cdot cm^{-1}$ at the wavelength of 990 nm (**Figure 2d**). These high extinction coefficient in the NIR region enable these SPs to efficiently utilize NIR photons. Therefore, the results indicate that both the molecular weights and alkyl side chain may play important roles in the aggregation ability and extinction coefficients of the SPs. These features have been proved beneficial for the transition of the infrared photon by eliminating the steric effect between the thiophene and BT units as well as the non-bond interaction between the sulfur of the thiophene and the nitrogen of the BT [45, 46]. Furthermore, the photothermal conversion capacity of SPs-encapsulated nanomedicine was comparatively analyzed in subsequent studies. The TIID-BT is the first SP which is optimized through molecular weight- and alkyl side chain-engineering, showing a great potential to be a photothermal agent in the biomedical area. Its high photothermal conversion efficiency in the NIR-II range is conductive to kill deep tumor tissues due to the deep penetration ability of the NIR-II laser.

3.2 Synthesis and characterization of pH-sensitive DOX-conjugated copolymer

To improve the bioavailability of hydrophobic SPs and co-deliver with chemotherapeutic drug, a DOX-grafted block polymer monomethoxypoly(ethylene glycol)-poly(N-(N’,N’-diisopropylaminoethyl)-*co*-benzylamino-*co*-DOX)aspartamide (PEG-PAsp(DIP-BzA-DOX), referred to here as PADD) was prepared (**Figure 1** and **Scheme S3**). The characterization of PADD polymers was performed by ^{1}H-NMR and Fourier-transform infrared spectroscopy (FTIR). The disappearance of the peak at

5.05 ppm in the ^{1}H-NMR spectrum of PBLA was due to the aminolysis reaction between PBLA and BzA/DIP/ hydrazine (**Figure S8a** and **b**). The presence of BzA, DIP, and hydrazone bond were confirmed by ^{1}H-NMR peaks at 7.20 ppm (f’, $-CONHCH_3Ph$), 0.95 ppm (k’, $-CONHCH_2CH_2C(CH_3)_2$), and 4.25 ppm (r’, $-N-NH_2$) (**Figure 3a** and **S8**), respectively. The DOX was conjugated to hydrazine by amidation reaction, which was confirmed by ^{1}H-NMR resonance peaks at 7.30, 7.61 and 7.95 ppm. The grafting densities of the DIP, BzA, and DOX were 43, 2, and 5, respectively.

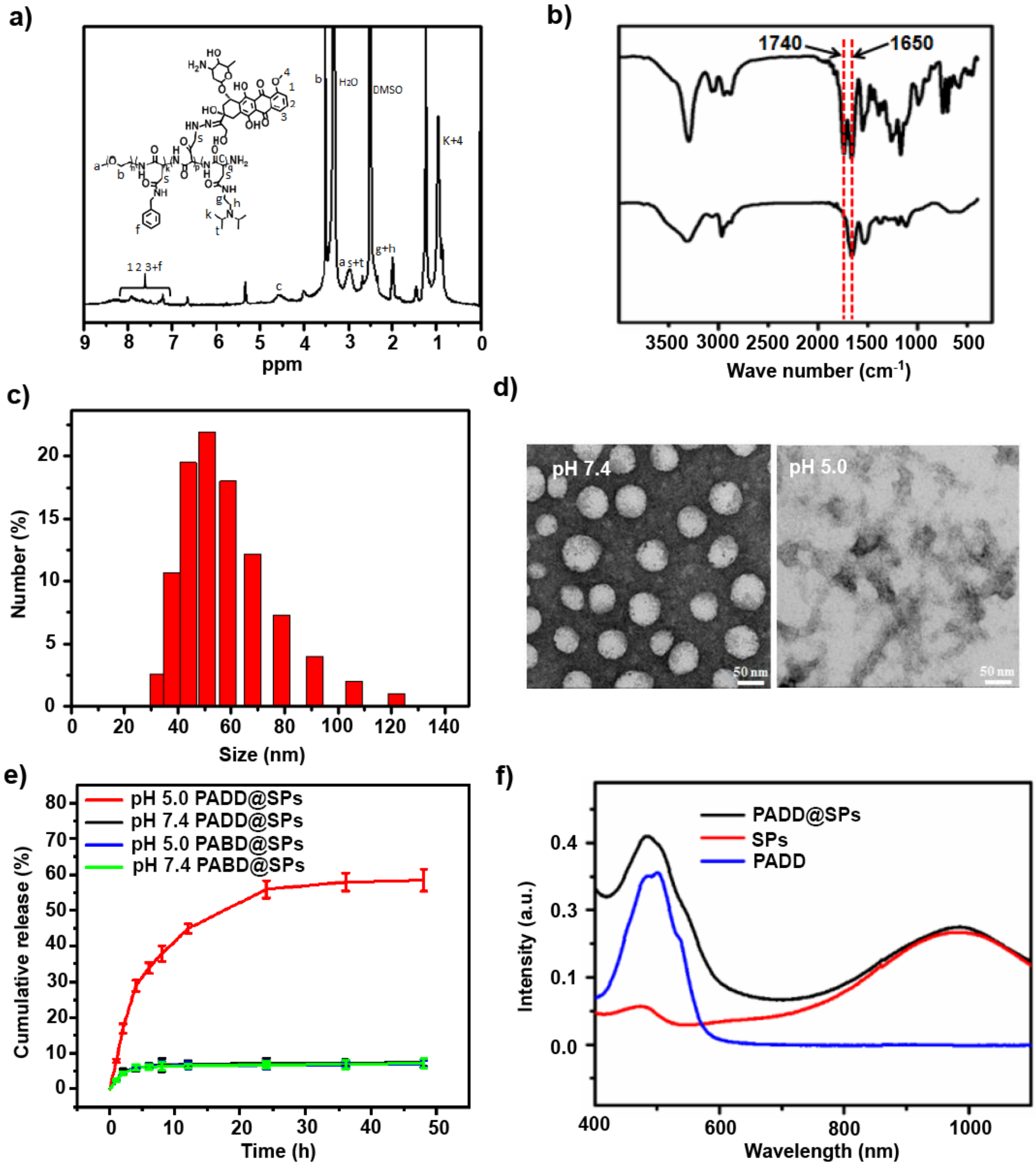

Figure 3. Preparation and characterization of amphiphilic polymers and nanoparticles. (a) PEG-PAsp(DIP-*co*-BzA-*co*-DOX) (PADD) polymer structure and ^{1}H-NMR analysis, (b) PADD polymer FT-IR analysis, (c) Size of PADD@SPs nanoparticles assembled with PADD polymers and SPs, (d) TEM images of

PADD@SP nanoparticles at pH 7.4 and 5.0, (e) *In vitro* DOX release profiles of pH-sensitive PADD@SPs and pH-insensitive PABD@SPs nanoparticles at different pH value and 37 ºC, and (f) UV-Vis-NIR absorption of PADD nanoparticles without SPs, SPs, and PADD@SPs nanoparticles, respectively. The data in e) are presented as the mean ± SD (n = 3), with the DOX loading content at 12 %. PABD@SPs indicates the nanoparticles assembled with PEG-PAsp(BzA-*co*-DOX) polymers and SPs.

3.3 Preparation and characterization of SP- and DOX-encapsulated nanoparticles

The nanoparticles assembled by the amphiphilic copolymer PADD and the semiconducting polymer (i.e., SP-C8, SP-C10, and L-SP-C10) exhibited a uniform and spherical morphology with a diameter of ~50 nm (**Figure 3c** and **d**). The zeta potential of PADD@SPs nanoparticles was +5.65 mV (**Table S2**), which favored the cellular uptake by tumor cells. The loading contents of DOX and SPs were 12.0% and 7.5%, and the loading efficiency of SPs was 62.1% (**Table S3**). The DOX conjugated to polyaspartamide backbone can drop from nanoparticles by breakage of hydrazone bond in response to the acidic condition of the lysosome. To confirm this low pH-triggered DOX release, PADD@SPs were put in a solution mimicking the acidic lysosome (pH 5.0). As shown in Figure 3e, most of the DOX (~60%) was released from the nanoparticles in 35 h. The TEM image under the condition of pH 5.0 indicated the nanoparticle disassembly (**Figure 3d**). When DIP moieties were removed from block polymer in the nanoparticles assembled with PEG-PAsp(BzA-*co*-DOX) polymers and SPs (PABD), the DOX was hardly released from the PABD nanoparticles (**Figure 3e and S9**), indicating that both the DIP moiety and hydrazone bond were required to achieve a controlled release of DOX. The NIR irradiation had no significant effect on DOX release from PADD@SPs under the condition of pH 5.0 (**Figure S10**). The DOX was encapsulated in the hydrophobically micellar core composed of PAsp(DIP) and PAsp(BzA) blocks. In the condition of pH 5.0, although hydrophobic DIP moieties partially converted to hydrophilic ones, the BzA moieties kept the hydrophobic states, which may partially prevent the release of DOX. The dual optical absorption band of SPs-encapsulated PADD nanoparticles at 420-600 nm and 700-1100 nm is ascribed to the absorption of DOX and SP-C8 (**Figure 3f**), respectively. In contrast, the PADD nanoparticles without SPs just show a single absorption band of DOX at 420-600 nm. In addition, the PADD@SPs showed high serum stability (**Figure S11**).

3.4 Photothermal conversion of nanoparticles loaded with SPs

The temperature of the solution containing PADD@SPs rapidly and remarkably rose over time and reached up to 58.9 °C due to the balance between the NIR-induced heating and thermal dissipation by environment (**Figure S12**). These results indicated that the SPs could effectively convert NIR photons to thermal heat. Compared to the PADD@L-SP-C10 and PADD@SP-C10, the PADD@SP-C8 exhibited faster and higher temperature increase when exposed to the NIR irradiation (**Figure 4a-c** and **S12**). The time constant for heat transfer (τ_s) and photothermal conversion efficiency (η_T) are two important factors to assess photothermal materials, representing the temperature increase rate and light use capacity [43]. Compared to PADD@L-SP-C10, PADD@SP-C10 showed shorter τ_s (249.7 s vs. 256.4 s) and higher η_T (40.7% vs. 35.4%) likely due to the lower optical bandgap and higher extinction coefficient of SP-C10 [8]. The PADD@SP-C8 with short alkyl side chains exhibited better photothermal performance in term of τ_s (248.0 s vs. 249.7 s) and η_T (45% vs. 40.7%) than PADD@SP-C10 with long alkyl side chains, which may be due to better π–π stacking, planar, and increased mobility of carriers in SP-C8. Besides, the random grafting of DIP, BzA and DOX resulted in a more uniform microstructure than order block, which is theoretically in favor of the controlled release of DOX [47]. Thus, the PADD@SP-C8 was used in the subsequent experiments, referred to here as PADD@SPs.

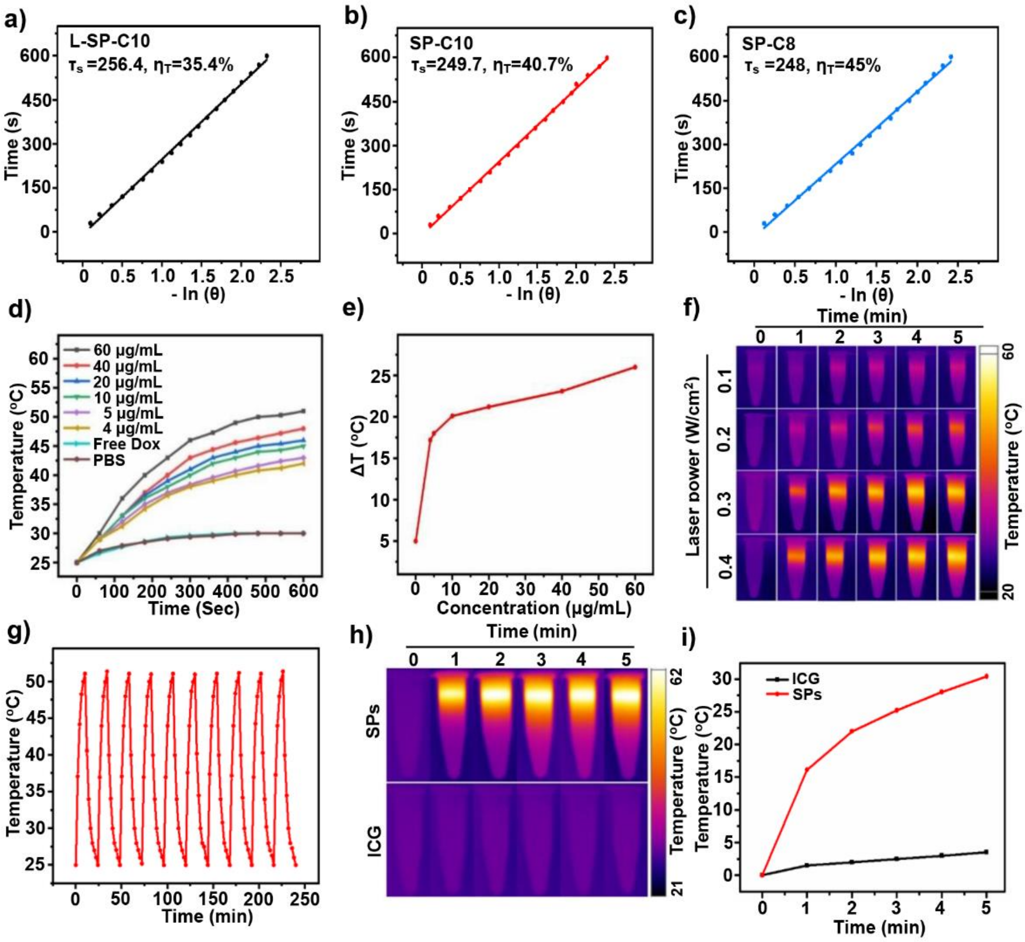

Figure 4. ***In vitro*** **photothermal properties of PADD@SPs.** (a)-(c) Photothermal conversion efficiencies of different types of SPs (L-SP-C10, SP-C10, and SP-C8) calcualted according to the linear correlations of cooling times against negative natural logarithm of driving force temperature, (d) Photothermal heating, (e) Time-dependent temperature change curves of different amounts of PADD@SPs nanoparticles under 980 nm laser irradiation at a power density of 0.3 W/cm^2, (f) Thermo-graphic images of PADD@SPs solutions (60μg/mL) irradiated with 980 nm laser for 5 min at different power of 0.1,0.2,0.3,0.4 W/cm^2, respectively, (g) Stability of PADD@SPs under laser on/off irradiation cycles at a power density of 0.3 W/cm^2, and a concentration of SP and DOX of 60 μg/mL and 120 μg/mL, respectively, (h) and (i) Comparison of photothermal properties of SP and ICG under laser irradiation at a power density of 0.3 W/cm^2, with a concentration of SP and ICG of 70 μg/mL. Except for the SPs in (a) and (b), the SP-C8 was used if applied.

Next, we evaluated the SP/NIR-mediated photothermal conversion. The solutions containing free DOX or PBS generated a slight increase of temperature by 5 °C when irradiated with NIR at a power density of 0.3 W/cm^2. In contrast, the PADD@SPs remarkably increased the temperature by 26 °C in a dose-dependent manner. After PADD@SPs solutions at 4, 5, and 10 μg/mL were irradiated with NIR for 300 sec, their temperatures increased by 13.0, 13.4, and 15.0 °C (**Figure 4d**), respectively. The appropriative temperature range of 45-50 °C for thermal antitumor therapy [48] was easily achieved even at low concentration of SP-C8 (4 μg/mL) and low power of NIR irradiation (0.3 W/cm^2) under a body temperature of 37 °C (**Figure 4d** and **e)**. Then, we analyzed the combined effect of NIR power level and irradiation time on the temperature change by thermal imaging (**Figure 4f**). Results indicated that the temperature of PADD@SPs solution increased with the increase of NIR power level and irradiation time, and the temperature change of nanoparticles solutions at a power level of 0.3 W/cm^2 showed no significant difference with that of 0.4 W/cm^2 under various irradiation times. The NIR irradiation of 980 nm laser at 0.3 W/cm^2 for 5 min caused no skin lesion. After ten heating-cooling cycles, the temperature pattern of SPs under NIR irradiation at 0.3 W/cm^2 remained unchanged (**Figure 4g**), indicating that PADD@SPs exhibited high photostability. ICG is an FDA-approved photothermal biomedical material due to its high thermal conductivity. At a power level of 0.3 W/cm^2 for 5 min, NIR irradiation increased temperature by ~3 °C for ICG but by ~28 °C for PADD@SPs (**Figure 4h** and **i**). The ICG and other reported semiconducting polymers receiving NIR irradiation at 1~2 W/ cm^2 for 5 min increased the temperature by ~22 °C [49, 50]. Moreover, the results in phantom experiments showed that the PADD@SPs/NIR-II (980 nm) irradiation was more effective than PADD@ICG/NIR-I (808 nm) system in deep tissues (**Figure S13**) because of the deeper tissue penetration depth of 980 nm laser than the 808 nm laser. These results demonstrate that the PADD@SPs may possess promising potentials and applications in photothermal therapy due to their high photothermal conversion efficiency at the relatively low power level of NIR irradiation [51]. Therefore, the conditions of NIR irradiation of 980 nm at 0.3 W/cm^2 for 5 min and SPs at 4 μg/mL were used in further study.

3.5 *In vitro* delivery and intracellular distribution of SPs and DOX

To track the intracellular distribution of SP, the coumarin-6 (Cr6) was used in lieu of the SPs. At 6 h post-incubation with PADD@SPs, the red fluorescence of DOX and green fluorescence of Cr6 colocalized in the cytoplasm, and merged into the yellow color (**Figure 5a**), indicating that the DOX and Cr6 were effectively co-delivered into the tumor cells. At 24 h after incubation, the DOX fluorescence was observed in the nuclei, implying that the DOX detached from nanoparticles and bound with nucleic acid in the nuclei. The co-delivery efficiency of DOX and Cr6 to A549 was quantified to be 92.12% using the flow cytometry assay (**Figure 5b**). In the pH-insensitive PABD nanoparticles (PABD NPs) without DIP moieties, the DOX could not be observed in the nuclei, suggesting that the DOX may not be released from nanoparticles, which was consistent with the results of *in vitro* drug release. The changes in temperature of cells receiving pH-sensitive PADD@SPs and completely pH-insensitive PEG-PCL@SPs were similar, indicating that the disassembly of nanoparticles in the lysosome hardly affected the photothermal conversion (**Figure S14**).

3.6 *In vivo* delivery and biodistribution of SPs and DOX

To further investigate the *in vivo* distribution of intravenously injected PADDs@SPs nanoparticles, the NIR fluorescent dye 1,1-dioctadecyl-3,3,3,3-tetramethylindotricarbocyanine iodide (DiR) was used in lieu of the SP. The fluorescence intensity of DiR in the tumor tissue reached a maximum value at 6 h after injection (**Figure 5c**). The highest fluorescence intensity of DiR was observed in an excised tumor compared to other excised organs including the heart, liver, spleen, lung, and kidney (**Figure 5d**). The accumulation of nanoparticles in the tumor was also confirmed by thermal and photoacoustic imaging (**Figure 5e and f**). The strongest photoacoustic signal was recorded at 6 h after nanoparticles injection (**Figure 5e**), consistent with the previously mentioned result of fluorescence imaging. At 12 h after nanoparticles injection, the tumor tissues receiving pH-sensitive nanoparticles (PADD@SPs) and pH-insensitive nanoparticles (PEG-PCL@SPs) showed a similar thermal signal intensity when irradiated with NIR for various times, again suggesting that the low pH-triggered nanoparticle disassembly had no influence on photothermal conversion (**Figure 5f**). Notably, the SP/NIR-generated hyperthermia can drive DOX penetration inside the deep tumor tissue (**Figure 5g**), which was in favor of killing the survived tumor cells in the photothermal therapy [4]. The tumor tissues from the mice receiving PADD@SPs with/without NIR irradiation were recorded using CLSM to quantitatively characterize the DOX penetration in the tumor tissue. The blood vessels were fluorescently marked green. Although it gradually weakened with the increased distance from the blood vessel, the intensity of DOX fluorescence of ~60 a.u. was recorded at the 80 μm from the blood vessel in the tumor tissue from the mice receiving PADD@SPs injection plus NIR irradiation (**Figure S15**). On the contrary, the tumor tissue section from mice injected with PADD@SPs but no NIR irradiation showed much weaker DOX fluorescence intensity in the vicinity of the blood vessel. These results indicate that the photothermal therapy based on PADD@SPs with NIR irradiation could promote DOX penetration in the tumor tissue to kill tumor cells that survived the photothermal therapy.

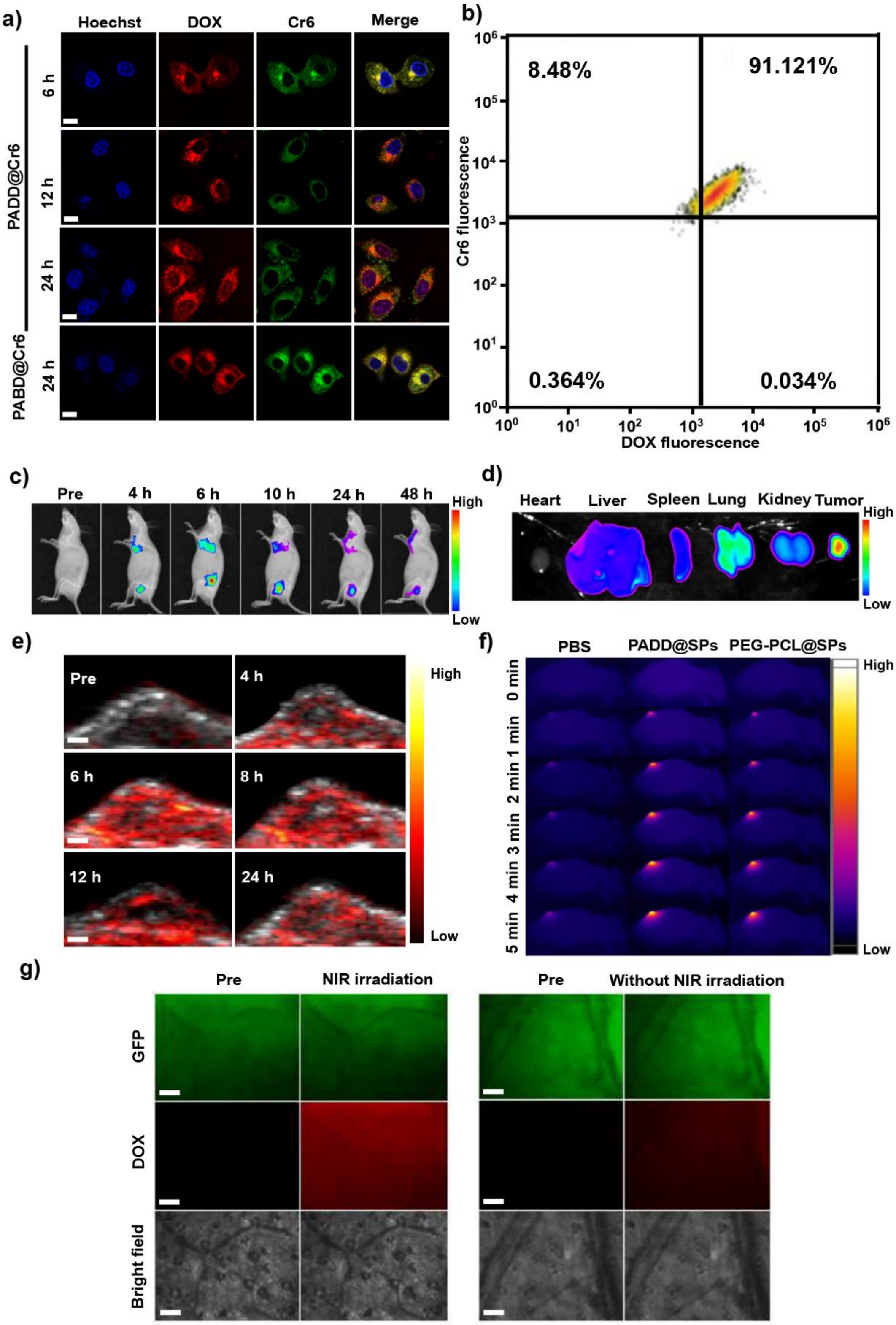

Figure 5. Tumor cell uptake, *in vivo* imaging, and intratumoral penetration of nanoparticles. (a) Confocal laser scanning microscope (CLSM) of A549 cells treated with PADD@Cr6 and PABD@Cr6 nanoparticles, where nuclei were stained

blue with Hoechst 33324; DOX emitted red fluorescence; Coumarin 6 (Cr6) in lieu of SPs emitted green fluorescence, (b) Co-delivery efficiency of Cr6 and DOX in PADD@Cr6-treated A549 cells, (c) Biodistribution of PADD@Dir in A549 xenograft mice, where dialkylcarbocyanines (Dir) dye was used to substitute SPs for monitoring nanoparticles, and the white arrows indicate tumor site, (d) Dir fluorescence signal in major organ excised from A549 xenograft mice, where the dose of DiR was 1 mg/kg body weight, (e) Thermal images of A549 xenograft mice irradiated with 980 nm laser at 6 h after injection of 200 µL of PADD@SPs, PEG-PCL@SPs, and PBS, (f) Photoacoustic images of A549 xenograft mice at various time points after intravenous injection of PADD@SPs nanoparticles (200 µL), and (g) *In vivo* CLSM of A549-GFP tumor subcutaneously implanted at auricle area of mice. The A549-GFP tumor cells and DOX were directly imaged at an 8 h time point after PADD@SPs nanoparticles injection. The NIR irradiation was performed at a 6 h time point after injection. If applied, NIR irradiation was performed for 5 min at a power density of 0.3 W/cm^2. In the Pre group, the mice were imaged before PADD@SPs injection. The concentration of SPs was 2 mg/kg body weight. The scale bars are 10 µm in the panel (a), 1 mm in the panel (e), and 100 µm in the panel (g).

3.7 *In vitro* synergistic effect of PADD@SPs-mediated combinatorial therapy

The co-delivery of DOX and SP has provided feasible nanoplatforms to achieve combination of photothermal therapy and chemotherapy, with a synergistic effect strengthened by controlled release and intratumoral penetration of DOX. As shown in **Figure 6a**, the nanoparticles (i.e., PADB NPs and PADB@SPs) without DOX and NIR irradiation showed no cytotoxicity to A549 cells. The PADD@SPs and PADD NPs treatments lacking NIR irradiation had no significant difference in cytotoxicity (IC_{50} = 14 µg/mL) to A549 cells (**Figure 6b**). The increase of NIR laser power slightly increased the cytotoxicity of PADB@SPs/NIR treatment lacking DOX. In contrast, the combined treatment (PADD@SPs/NIR treatment) of SP-based photothermal therapy (4 µg/mL) and DOX-based chemotherapy (8 µg/mL) remarkably decreased the cell viability to 38% from the original values of 70.6% and 70.1% compared to single-method treatments (PADD@SPs and PADB@SP/NIR treatments) (**Figure 6C**). Although the 8 µg/mL free DOX would have minimal effect on the cell viability, the nanoformulation of DOX could enhance cellular apoptosis by 30 folds at much lower DOX concentration than free DOX [37], which may be attributed to the fact that nanomedicine can effectively bypass the drug efflux pump pathway. In addition, the use of low DOX concentration can reduce the potential for DOX-induced cardiotoxicity which is dose-dependence [52]. Notably, the combined treatment (PADD@SPs/NIR) at a concentration of 8 μg/mL DOX and 4 μg/mL SPs showed a CI value of 0.429 (**Figure S16b**), indicating that the PADD@SPs/NIR treatment could synergistically kill tumor cells [44]. In addition, the PABD NPs treatment that is lacking DIP groups showed no significant cytotoxicity to A549 cells because the DOX was trapped in the hydrophobic core of micelles (**Figure S16C**). The synergistic effect of the PADD@SPs-mediated drug co-delivery was confirmed by flow cytometry assay (Figure 6d). Free DOX treatment caused only a few apoptotic cells (18.4%). The nano-formulations of DOX alone (PADD NPs treatment with DOX but lacking SPs and NIR irradiation) showed no clear difference in the percentage of apoptotic cells (34.3% vs. 33.1%) with PADD@SPs treatment loading both DOX and SPs but lacking NIR irradiation. The PADB@SPs/NIR treatment in the presence of SPs and NIR irradiation (but lacking DOX) resulted in apoptotic cells of 63.8%. The combined treatment of PADD@SPs/NIR enhanced the percentage of apoptotic cells up to 84.7%. These results demonstrate that the co-delivery of SPs and DOX induces more apoptotic tumor cells. The two pH-sensitive structures, including hydrazone bond and DIP moiety, resulted in a rapid DOX release in response to the acidic lysosomal environment, which could help to enhance the synergistic effect of drugs.

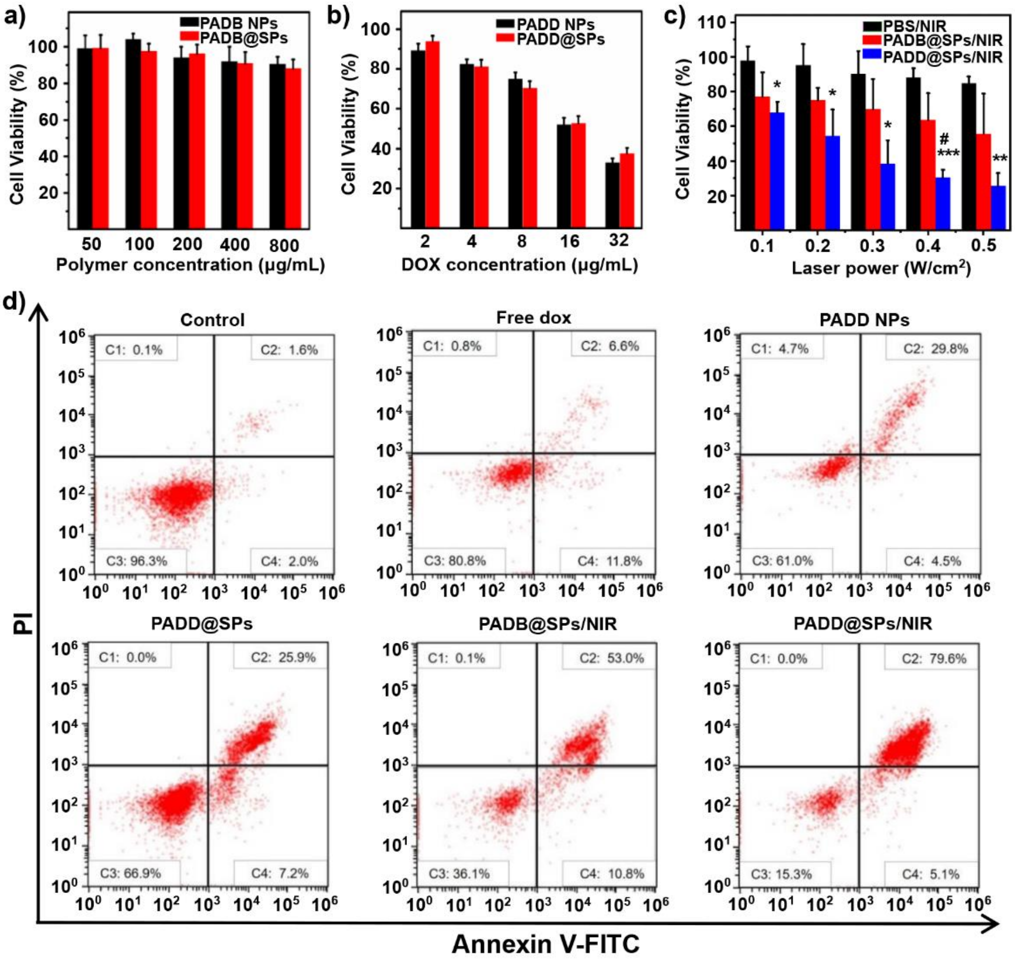

Figure 6. ***In vitro* synergistic effect of nanoparticles on cell viability and apoptosis**. Cell viabilities to A549 cells of (a) Nanoparticles lacking DOX (PADB@SPs and blank PADB NPs) without NIR irradiation, (b) DOX-conjugated nanoparticles (PADD@SPs and blank PADD NPs without SPs) without NIR irradiation, and (c) SP-encapsulated nanoparticles with/without DOX (PADB@SPs and PADD@SPs) under NIR irradiation at different power densities for 5 min. Error bars indicate standard deviations of three separate measurements. $^{*}p$ <0.05, $^{**}p$ <0.01, and $^{***}p$ < 0.001 compared with PBS plus NIR irradiation treatment; $^{\#}p$ <0.05 compared with PADB@SPs with NIR irradiation treatment. The PADB@SPs and blank PADB NPs were prepared with PEG-PAsp(DIP-*co*-BzA) polymers (PADB polymers) with or without SPs. (d) Flow cytometry analysis of cell apoptosis, where C1: necrotic cells; C2: late apoptotic cells; C3: normal viable cells; C4: early apoptotic cells; DOX concentration if applied is 8 μg/mL; and SPs concentration if applied is 4 μg/mL. If required, NIR irradiation was performed at a power density of 0.3 W/cm^2 for 5 min.

3.8 *In vivo* synergistic antitumor effect of PADD@SPs-mediated combinatorial therapy

Based on previous results, we further investigated whether PADD@SPs-based combinatorial therapy could act synergistically to reduce tumor growth *in vivo*. Compared to the free DOX, the nano-formulations of DOX (PADD NPs and

PADD@SPs) reduced the tumor volumes by ~37.5% at 27 days after intravenous nanoparticles injection, and showed no clear difference with PADB NPs/NIR irradiation treatment. In contrast, the tumor volume of mice treated with PADD@SPs/NIR irradiation shrank to half of its original size at 30 days after nanoparticles injection and resulted in the increase of the mice survival rate and survival time.

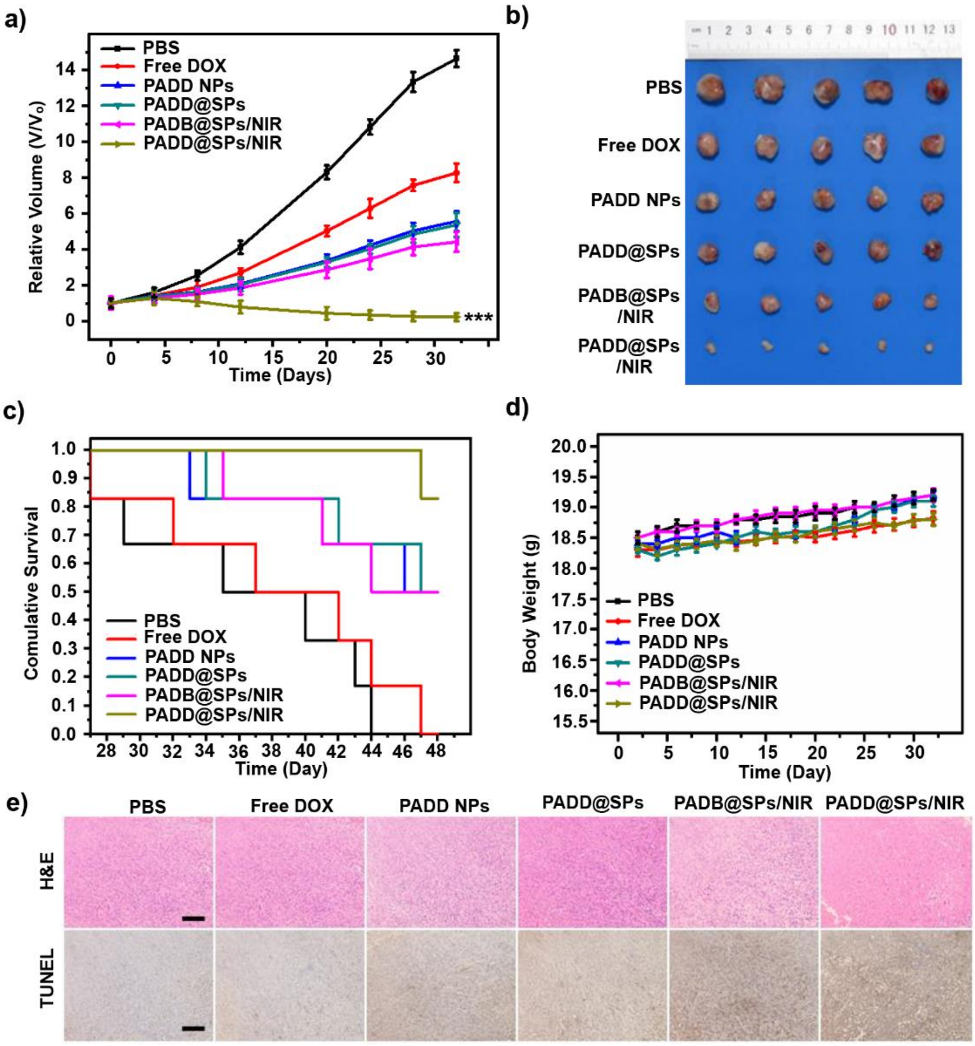

Figure 7. *In vivo* antitumor activity of combined photodynamic therapy and chemotherapy. (a) Tumor growth, (b) excised tumor tissues in A549 xenograft tumor -bearing mice after tail injection of various nanoparticles with or without NIR irradiation, (c) Survival rate, and (d) body weight of A549 xenograft tumor-bearing mice in Panel a). Data are present as the mean with a standard deviation (n=6), $^{**}p<0.01$, and $^{***}p<0.001$. (e) H&E and TUNEL analyses of tumor sections from A549 xenograft mice reviving various treatments. If applied, doses of SPs and DOX were 2 and 4 mg/kg, respectively. The scale bar is 200 μm.

All mice treated with the free DOX and PBS treatments died at 47 days after the first drug injection. The single DOX-induced chemotherapy (i.e., PADD NPs and PADD@SPs treatments) and single SPs/NIR-mediated photothermal therapy (i.e., PADB@SPs/NIR treatment) resulted in 50% mice survival to >48 days. The combined treatment in the presence of NIR (PADD@SPs/NIR) prolonged the survival rate by 83%, to >48 days. The body-weight of mice receiving PADD@SPs/NIR treatment was similar to that of the PBS control group. The survival study was stopped when the tumor volumes reached above 1500 mm^3 according to the regulations of the Animal Care and Use Committee of Sun Yat-Sen University. Moreover, the greatest apoptotic and necrotic tumor cells were observed in the tumor tissues from mice treated with PADD@SPs plus NIR irradiation according to the H&E and TUNEL analyses (**Figure 7e**). The tumor temperature rapidly increased up to ~50 °C within 5 min when irradiated with laser after intravenous injection of PADB@SPs and PADD@SPs (**Figure S17**). By contrast, the temperatures of tumor sites of mice treated with PBS, free DOX, and PADD NPs kept at ~39 °C even under the NIR irradiation for 5 min. These results indicate the SPs/NIR-generated hyperthermia is closely related to the tumor cell apoptosis and necrosis. In addition, major organs (i.e., heart, liver, spleen, lung, and kidney) from mice treated with PADD@SPs plus NIR irradiation showed similar structures as that of PBS-treated control group (**Figure S18**). These results demonstrated that the co-delivery of SP and DOX by pH-sensitive amphiphilic polymer plus NIR irradiation achieved a synergistic antitumor effect. Although some multifunctional nanosystems have been reported to synergistically enhance antitumor outcomes, the microenvironment-responsive nanocarrier regarding co-deliver the SPs and the chemotherapeutic drugs is rarely reported. The PADD@SPs-based nanosystem possesses several advantages. First, the DOX-conjugation to the polymer through a pH-sensitive bond is favorable to enhance DOX loading content and achieve on-demand drug release. Second, the pH-sensitive micellar cores of PADD@SPs not only stabilize the nanoparticles in physiological condition but also promote drug release through micelle disassembly in response to the acidic microenvironment of lysosome in tumor cells. Third, the SPs/NIR-generated hyperthermia drives drug penetration inside the tumor tissue.

4. Conclusions

The photothermal conversion efficiency of the semiconducting polymer was improved by optimizing the backbone and alkyl side chain. The SP with a long backbone but short alkyl side chain showed enhanced planarity and increased mobility of carriers, resulting in high photothermal conversion efficiency. The amphiphilic copolymer with two pH-sensitive structures was used to co-deliver SPs and DOX. The pH-sensitive hydrazine bond and DIP moiety allowed the rapid cytoplasmic release of DOX, which was drove to deep sites of the tumor tissue by SP/NIR-generated hyperthermia, killing tumor cells that survived from photothermal therapy. Under NIR irradiation, the combination of SPs and DOX delivery approach exhibited a synergistic antitumor effect, compared to the result of any single drug treatment. Overall, this combination of improved photothermal biomedical material and chemotherapeutic drug using multifunctional carrier possesses several advantages and shows great potential in antitumor therapy.

Declaration of competing interest

There are no conflicts to declare.

Acknowledgement

This work was supported by the National Natural Science Foundation of China (21875289 and 21875291), the Guangdong-Hong Kong Joint Innovation Project (2016A050503026), the Major Project on the Integration of Industry, Education and Research of Guangzhou City (201704030123).

Data availability

The authors declare that all data supporting the results of this study are available in the paper and its supplementary data files. The related raw data and detailed protocols can be available from the corresponding author.

References

[1] Y. Jiang, K. Pu, Advanced photoacoustic imaging applications of near-Infrared absorbing organic nanoparticles, Small 13 (30) (2017) 1700710.

[2] C. Xie, X. Zhen, Q. Miao, Y. Lyu, K. Pu, Self-assembled semiconducting polymer nanoparticles for ultrasensitive Near-Infrared afterglow imaging of metastatic tumors, Adv. Mater. 30 (21) (2018) 1801331.

[3] Z. Yang, X. Chen, Semiconducting perylene diimide nanostructure: multifunctional phototheranostic nanoplatform, Acc. Chem. Res. 52 (5) (2019) 1245-1254.

[4] G. Zhou, H. Xiao, X. Li, Y. Huang, W. Song, L. Song, M. Chen, D. Cheng, X. Shuai, Gold nanocage decorated pH-sensitive micelle for highly effective photothermo-chemotherapy and photoacoustic imaging, Acta Biomater. 64 (2017) 223-236.

[5] H. Zhu, P. Cheng, C. Peng, K. Pu, Recent progress in the development of near-infrared organic photothermal and photodynamic nanotherapeutics, Biomater Sci. 6 (2018) 746-765.

[6] Q. Chen, L. Feng, J. Liu, W. Zhu, Z. Dong, Y. Wu, Z. Liu, Intelligent albumin−MnO2 nanoparticles as pH-/H2O2-responsive dissociable nanocarriers to modulate tumor hypoxia for effective combination therapy, Adv. Mater. 28 (33) (2016) 7129-7136.

[7] B. Smma, A. Sv, B. Tma, B. Skda, External stimulus responsive inorganic nanomaterials for cancer theranostics, Adv. Drug Deliv. Rev. 138 (2019) 18-40.

[8] Q. Miao, C. Xie, X. Zhen, Y. Lyu, H. Duan, X. Liu, J.V. Jokerst, K. Pu, Molecular afterglow imaging with bright, biodegradable polymer nanoparticles, Nat. Biotechnol. 35 (11) (2017) 1102-1116.

[9] F. Ding, Y. Zhang, X. Lu, Y. Sun, Recent advances of Near-Infrared II fluorophores for multifunctional biomedical imaging, Chem. Sci. 9 (2018) 4370-4380.

[10] J. Li, K. Pu, Development of organic semiconducting materials for deep-tissue optical imaging, phototherapy and photoactivation, Chem. Soc. Rev. 48 (1) (2019) 38-71.

[11] J. Li, K. Pu, Semiconducting polymer nanomaterials as Near-Infrared photoactivatable protherapeutics for cancer, Acc. Chem. Res. 53 (4) (2020) 752-762.

[12] J. Li, R. Jiang, Q. Wang, X. Li, X. Hu, Y. Yuan, X. Lu, W. Wang, W.Huang, Q. Fan, Semiconducting polymer nanotheranostics for NIR-II/Photoacoustic imaging-guided photothermal initiated nitric oxide/photothermal therapy, Biomaterials. 217 (2019) 119304.

[13] Y. He, Y. Cao, Y. Wang, Progress on Photothermal conversion in the second NIR Window based on conjugated polymers, Asian J. Org. Chem. 7 (11) (2019) 2201-2212.

[14] Y. Jiang, J. Huang, C. Xu, K. Pu, Activatable polymer nanoagonist for second near-infrared photothermal immunotherapy of cancer, Nat. Commun. 12 (1) (2021) 742.

[15] S. He, Y. Jiang, J. Li, K. Pu, Semiconducting Polycomplex Nanoparticles for Photothermal Ferrotherapy of Cancer, Angew. Chem. Int. Ed. 59 (26) (2020) 10633-10638.

[16] Z. Zeng, C. Zhang, J. Li, D. Cui, Y. Jiang, K. Pu, Activatable Polymer Nanoenzymes for Photodynamic Immunometabolic Cancer Therapy, Adv. Mater. 33 (4) (2021) 2007247.

[17] C. Xu, K. Pu, Second near-infrared photothermal materials for combinational nanotheranostics, Chem. Soc. Rev. 50 (2021) 1111-1137.

[18] Y. He, W.Yue, Y. Wang, Coupling molecular rigidity and flexibility on fused backbones for NIR-II photothermal conversion, Chem. Sci. 12 (2021) 5177-5184.

[19] Y. Yu, Y. Fang, Q. Miao, X. Zhen, D. Ding, K. Pu, Intraparticle molecular orbital engineering of semiconducting polymer nanoparticles as amplified theranostics for in vivo photoacoustic

imaging and photothermal therapy, ACS Nano. 10 (4) (2016) 4472-4481.

[20] R.S. Ashraf, A.J. Kronemeijer, D.I. James, H. Sirringhaus, I. Mcculloch, A new thiophene substituted isoindigo based copolymer for high performance ambipolar transistors, ChemComm. 48 (33) (2012) 3939-3941.

[21] Y. Wang, Y. Yu, H. Liao, Y. Zhou, W. Yue, The chemistry and applications of heteroisoindigo units as enabling links for semiconducting materials, Acc. Chem. Res. 53 (12) (2020) 2855-2868.

[22] Y. Cao, J. Dou, N. Zhao, S. Zhang, Y. Zheng, J. Zhang, J. Wang, J. Pei, Y. Wang, Highly efficient NIR-II photothermal conversion based on an organic conjugated polymer, Chem. Mater. 29 (2) (2016) 718-725.

[23] T. Lei, Y. Cao, Y. Fan, C. Liu, S. Yuan, J. Pei, High-performance air-stable organic field-effect transistors: isoindigo-based conjugated polymers, J. Am. Chem. Soc. 133 (16) (2011) 6099–6101.

[24] T. Lei, J. Dou, P. Jian, Influence of alkyl chain branching positions on the hole mobilities of polymer thin-film transistors, Adv. Mater. 24 (48) (2012) 6457-6461.

[25] H. Rang, M.A. Uddin, C. Lee, K.H. Kim, T.L. Nguyen, W. Lee, Y. Li, W. Cheng, Y.W. Han, B.J. Kim, Determining the role of polymer molecular weight for high-performance all-polymer solar cells: its effect on polymer aggregation and phase separation, J. Am. Chem. Soc. 137 (6) (2015) 2359-2365.

[26] W. Yue, R.S. Ashr Af , C.B. Nielsen, E. Collado-Fregoso, M.R. Niazi, S.A. Yous Af , M. Kirkus, H.Y. Chen, A. Amassian, J.R. Durrant, A thieno[3,2-b][1]benzothiophene isoindigo building block for additive- and annealing-free high-performance polymer solar cells, Adv. Mater. 27 (32) (2015) 4702-4707.

[27] X. Wu, E. Yeow, Tuning the NIR downconversion luminescence and photothermal conversion efficiencies of MNdxY1−xF4 (M = Na and Li) nanocrystals for use in anti-counterfeiting labels with opposite displays, Nanoscale. 32 (11) (2019) 15259-15269.

[28] Z. Wang, U. Kumar, X. Zhen, R. Zhang, Y. Jiang, X. Ai, Z. Zhang, M. Hu, Z. Meng, Y. Lu, pH-sensitive and biodegradable charge-transfer nanocomplex for second near-infrared photoacoustic tumor imaging, Nano Res. 12 (2019) 49-55.

[29] Y. Yang, X. Fan, L. Li, Y. Yang, W. Huang, Semiconducting polymer nanoparticles as theranostic system for near-infrared II fluorescence imaging and photothermal therapy under safe laser fluence, ACS Nano. 14 (2) (2020) 2509-2521.

[30] P. Chen, Y. Ma, Z. Zheng, C. Wu, G. Liang, Facile syntheses of conjugated polymers for photothermal tumour therapy, Nat. Commun. 10 (1) (2019) 1192.

[31] L. Wang,Y. yuan,X. Shuai,Photothermo-chemotherapy of cancer employing drug leakage-free gold nanoshells, Biomaterials. 78 (2016) 40-49.

[32] L. Zhang, Y. Zhang,Y. Xue,C. Zhang, Transforming weakness into strength: photothermal-therapy-induced inflammation enhanced cytopharmaceutical chemotherapy as a combination anticancer treatment, Adv. Mater. 31 (5) (2018) 1805936.

[33] W. Cheng, J. Nie, N. Gao, G. Liu, W. Tao, X. Xiao, L. Jiang, Z. Liu, X. Zeng, L. Mei, A multifunctional nanoplatform against multidrug resistant cancer: merging the best of targeted chemo/gene/photothermal therapy, Adv. Funct. Mater. 27 (45) (2017) 1704135.1-1704135.15.

[34] W. Li, J. Peng, L. Tan, W. Jing, Z. Qian, Mild photothermal therapy/photodynamic therapy/chemotherapy of breast cancer by lyp-1 modified docetaxel/IR820 co-loaded micelles, Biomaterials. 106 (2016) 119-133.

[35] Y. Zhang, L. Feng, J. Wang, D. Tao, C. Liang, L. Cheng, E. Hao, Z. Liu, Surfactant-sripped

micelles of near infrared dye and paclitaxel for photoacoustic imaging guided photothermal-chemotherapy, Small. 14 (44) (2018) 1802991.

[36] S. Deng, X. Li, S. Liu, J. Chen, D. Cheng, Codelivery of CRISPR-Cas9 and chlorin e6 for spatially controlled tumor-specific gene editing with synergistic drug effects, Sci Adv. 6 (29) (2020) eabb4005.

[37] D. Cheng, N. Cao, J. Chen, X. Yu, X. Shuai, Multifunctional nanocarrier mediated co-delivery of doxorubicin and siRNA for synergistic enhancement of glioma apoptosis in rat, Biomaterials. 33 (4) (2012) 1170-1179.

[38] H. Xiao, Y. Guo, B. Li, X. Li, X. Shuai, M2-like tumor-associated macrophage-targeted codelivery of STAT6 inhibitor and IKKβ siRNA induces M2-to-M1 repolarization for cancer immunotherapy with low Immune side effects, ACS Cent. Sci. 6 (7) (2020) 1208-1222.

[39] W. Wang, D. Cheng, F. Gong, X. Miao, X. Shuai, Design of multifunctional micelle for tumor-targeted intracellular drug release and fluorescent imaging, Adv. Mater. 24 (1) (2012) 115-120.

[40] J. Dai, S. Lin, C. Du, S. Zou, X. Shuai, Interlayer-crosslinked micelle with partially hydrated core showing reduction and pH dual sensitivity for pinpointed intracellular drug release, Angew. Chem. Int. Ed. 50 (40) (2011) 9404-9408.

[41] H.Xiao,X.Li,C.Zheng,Q.Liu,C.Sun,J.Huang,Y.Wang,Y.Yuan, Intracellular pH-responsive polymeric micelle for simultaneous chemotherapy and MR imaging of hepatocellular carcinoma, J Nanopart Res. 22 (5) (2020) 1-15.

[42] T. Yin, P. Wang, J. Li, R. Zheng, B. Zheng, D. Cheng, R. Li, J. Lai, X. Shuai, Ultrasound-sensitive siRNA-loaded nanobubbles formed by hetero-assembly of polymeric micelles and liposomes and their therapeutic effect in gliomas, Biomaterials. 34 (18) (2013) 4532-4543.

[43] Y. Liu, K. Ai, J. Liu, M. Deng, L. Lu, Dopamine-melanin colloidal nanospheres: an efficient near-infrared photothermal therapeutic agent for in vivo cancer therapy, Adv. Mater. 25 (9) (2013) 1353-1359.

[44] T. Chou, Theoretical basis, experimental design, and computerized simulation of synergism and antagonism in drug combination studies, Pharmacol. Rev. 58 (3) (2006) 621-681.

[45] H. Huang, L. Yang, F. Antonio, Organic and polymeric semiconductors enhanced by noncovalent conformational locks, Chem. Rev. 117 (15) (2017) 10291-10318.

[46] Q. Wang, Y. Dai, J. Xu, J. Cai, X. Niu, L. Zhang, R. Chen, Q. Shen, W. Huang, Q. Fan, All-in-One phototheranostics: single laser triggers NIR-II fluorescence/photoacoustic imaging guided photothermal/photodynamic/chemo combination therapy, Adv. Funct. Mater. 29 (31) (2019) 1901480.1-1901480.12.

[47] L. Zhang, H. Xiao, J. Li, D. Cheng, X. Shuai, Co-delivery of doxorubicin and arsenite with reduction and pH dual-sensitive vesicle for synergistic cancer therapy, Nanoscale. 8 (2016) 12608-12617.

[48] Y. Kai, H. Xu, C. Liang, C. Sun, J. Wang, L. Zhuang, In Vitro and In Vivo Near-Infrared Photothermal Therapy of Cancer Using Polypyrrole Organic Nanoparticles, Adv. Mater. 24 (41) (2012) 5586-5592.

[49] Z. Cao, L. Feng, G. Zhang, J. Wang, X. Yang, Semiconducting polymer-based nanoparticles with strong absorbance in NIR-II window for in vivo photothermal therapy and photoacoustic imaging, Biomaterials. 155 (2018) 103-111.

[50] J. Zhang, Y. Miao, W. Ni, H. Xiao, J. Zhang, Cancer cell membrane coated silica nanoparticles loaded with ICG for tumour specific photothermal therapy of osteosarcoma, Artif Cells Nanomed Biotechnol. 47 (1) (2019) 2298-2305.

[51] X. Zhu, H. Wan, H. Jia, L. Liu, J. Wang, Porous pt nanoparticles with high Near-Infrared photothermal conversion efficiencies for photothermal therapy, Adv. Healthc. Mater. 5 (24) (2016) 3165-3172.

[52] C. Carvalho, R. Santos, X. Renato, S. Cardoso, S. Correia, P. Oliveira, M. Santos, P. Moreira, Doxorubicin: The Good, the Bad and the Ugly Effect, Curr Med Chem. 16 (25) (2009) 3267-3285.